Electronic Supplementary Information

Experiment Section

Materials: Sodium nitrate ($NaNO_3$), cobalt nitrate hexahydrate ($Co(NO_3)_2 \cdot 6H_2O$), boric acid (H_3BO_3), sodium nitroferricyanide dihydrate, and sulfanilamide were procured from Aladdin Industrial Co. Phosphoric acid (H_3PO_4), N-(1-naphthyl)ethylenediamine dihydrochloride, and hydrochloric acid (HCl) were acquired from Keshi Chemical Reagent Co. Salicylic acid, sodium nitrite ($NaNO_2$), and sodium citrate were sourced from Fuchen Chemical Reagent Co. Sodium hydroxide (NaOH) and p-dimethylaminobenzaldehyde were obtained from Macklin and CIVI Chemical Reagent Co., respectively. All chemicals were utilized without additional purification.

Preparation of B-Co_3O_4/TM: For the synthesis of B-Co_3O_4/TM, the hydroxide nanoarray precursor was initially prepared using an electrodeposition method. Employing a titanium mesh (TM, 1 × 1 cm^2) as the working electrode, a saturated calomel electrode (SCE) as the reference electrode, and Pt as the counter electrode, $Co(OH)_2$/TM was synthesized by electrodepositing in a 0.1 M $Co(NO_3)_2 \cdot 6H_2O$ solution (-1.0 V vs. SCE, 120 s). Subsequently, the $Co(OH)_2$/TM was subjected to multiple washes with ethanol and water, followed by drying at 60 °C. The resulting $Co(OH)_2$/TM was immersed in a 10 mM boric acid solution for 1 h, dried and annealed at 400 °C in a tube furnace for 2 h under an Ar atmosphere to obtain self-supporting B-doped Co_3O_4 (B-Co_3O_4/TM) nanosheet arrays. Additionally, Co_3O_4/TM was synthesized using the same method without soaking in boric acid solution, serving as a comparative sample.

Characterization: Morphology information of samples was unveiled through scanning electron microscopy (SEM, ZISS 300, 5.0 kV) and transmission electron microscopy (TEM, JEM-F200, JEOL Ltd.). The crystal structure of as-prepared materials was determined using X-ray diffraction (XRD, Philip D8) with Cu K_α source radiation at a scanning rate of 5° min^{-1} from 10 to 80°. Chemical compositions were analyzed using X-ray photoelectron spectroscopy (XPS, ESCALAB 250 Xi, Thermo Scientific) using

Al K_α source radiation with an energy of 1486.6 eV. Absorbance data from the spectrophotometer were obtained using Ultraviolet-visible (UV) spectrophotometer (Shimadzu UV-2700).

Electrochemical measurements: All electrochemical measurements were conducted within an H-type cell, separated by a treated Nafion 117 membrane, employing a CHI 760E electrochemical workstation (Shanghai, Chenhua). Electrolyte solution (30 mL) consisted of Ar-saturated 0.1 M NaOH, with and without 0.1 M NO_3^- ($NaNO_3$). The working electrode, counter electrode, and reference electrode were B-Co_3O_4/TM (0.5 × 0.5 cm^2), Pt, and Hg/HgO, respectively. According to the Nernst equation, all potentials were converted into the potential of the reversible hydrogen electrode (RHE) ($E_{RHE} = E_{Hg/HgO} + 0.059 \times pH + 0.098$ V). Linear sweep voltammetry (LSV) curves were measured by CHI 760E scans from 0 to −0.8 V in 0.1 M NaOH with and without 0.1 M NO_3^- at a scan rate of 10 mV s^{-1}. The potentiostatic experiment was carried out for 1 hour at each given potential, and the stirring speed was 200 rpm. During the experiment, Ar was continuously injected into the cathode chamber. In the cycle test, the potentiostatic test is performed at a stirring speed of 200 rpm at −0.7 V for 1 h, and then the next cycle used fresh electrolytes under the same conditions. All current densities presented in this work are based on the geometric surface area. The sampling method for the stability test is as follows: Before the test, a thin tube was inserted into H-cell and fixed below the electrolyte level. At each sampling time, 1 mL of electrolyte was pipetted into the centrifugal tube for subsequent testing.

Determination of NH_3: The yields of NH_3 in the electrolyte were calculated by spectrophotometer using the indophenol blue method. Concretely, 2 mL of the collected electrolyte after electrolysis mixed with 2 mL of 1 M NaOH solution containing 5% salicylic acid and 5% sodium citrate. Then, 1 mL of 0.05 M NaClO and 200 μL of 1 wt% sodium nitroferricyanide dihydrate were dropped in the collected electrolyte solution. The electrolytes of different potential and cycle tests were diluted 40 times, and the electrolytes of stability tests were diluted 200 times in H-cell. After maintained in the dark for 2 h, the concentration of NH_3 was identified by UV spectroscopy for a certain wavelength about 655 nm:

$$\mathrm{NH_3\ yield} = [\mathrm{NH_3}] \times V / (17 \times t \times A)$$

Where $[NH_3]$ is the mass concentration, V is the volume of the cathodic reaction electrolyte, t is the reduction time, and A is the area of the working electrode.

$$\mathrm{FE} = (n \times F \times c \times V) / (M \times Q)$$

Where F is the Faraday constant, n is the electrons transfer number, c is the calculated products concentration, V is the volume of the cathodic reaction electrolyte, M is the molecular mass of products, and Q is the total charge during electrosynthesis.

Determination of NO_2^-: The NO_2^- concentration was detected by the Griess test using UV spectrophotometry. The Griess reagent was provided through adding N-(1-naphthyl)ethylenediamine dihydrochloride (0.1 g), sulfanilamide (1.0 g), and H_3PO_4 (2.94 mL) in 50 mL H_2O. Typically, 1.0 mL Griess reagent was added to 1.0 mL electrolyte and 2.0 mL H_2O. After maintained for 10 min, the concentration of NO_2^- was measured by UV spectroscopy at a wavelength of 540 nm:

$$\mathrm{NO_2^-\ yield} = [\mathrm{NO_2^-}] \times V / (46 \times t \times A)$$

Where $[NO_2^-]$ is the mass concentration, V is the volume of the cathodic reaction electrolyte, t is the reduction time, and A is the area of the working electrode.

$$\mathrm{FE} = (n \times F \times c \times V) / (M \times Q)$$

Where F is the Faraday constant, n is the electrons transfer number, c is the calculated products concentration, V is the volume of the cathodic reaction electrolyte, M is the molecular mass of NO_2^-, and Q is the total charge during electrosynthesis.

Determination of H_2: Detection and quantification of H_2 were executed on a gas chromatograph system (Shimadzu GC-2014C) equipped with flame ionization detectors (FIDs), FID-methanizer, online auto-sampling system, and thermal conductivity detector.

NO_3^- isotopic labelling experiment: The generated NH_3 was verified by an isotope-labelled tracer experiment using 0.1 M $^{15}NO_3^-$ as a N source. After 1 h of electroreduction at −0.7 V, the electrolyte (2 mL) in the cathodic chamber was neutralized by HCl aqueous solution (1.2 M). After that, the neutralized electrolyte (500 μL) was mixed with deuterium oxide (D_2O, 50 μL). And the mixture was sealed into a nuclear magnetic resonance (NMR) tube (5 mm in diameter, 600 MHz) for further tests.

Computational details: First-principles calculations with spin-polarized were carried out using density functional theory (DFT) performed in the VASP package,[1] and the projector augmented wave (PAW) approach was used to describe the interaction between ionic core and valence electrons with a cutoff of 500 eV. Perdew-Burke-Ernzerhof functional (PBE) with semi-empirical corrections of DFT-D3 were employed to depict exchange-correlation functional effect by general gradient approximation (GGA).[2]

Modeled by the Co_3O_4 (311) facet with two terminations, the upper two layers were loosened, but the bottom two layers were secured. The spurious interaction was avoided by the 15 Å thickness of the vacuum region. U = 3.32 eV of Co 3d orbitals was used to perform the Hubbard U model.[3] According to the Monkhorst-Pack scheme, 3 × 3 × 1 special k-points were applied to optimize the structural configuration by the Brillouin zone.[4] The force convergence thresholds and total energy are 0.02 eV/Å and less than 1×10^{-5} eV, respectively. Based on VASPKIT software, DFT results were explained.[5]

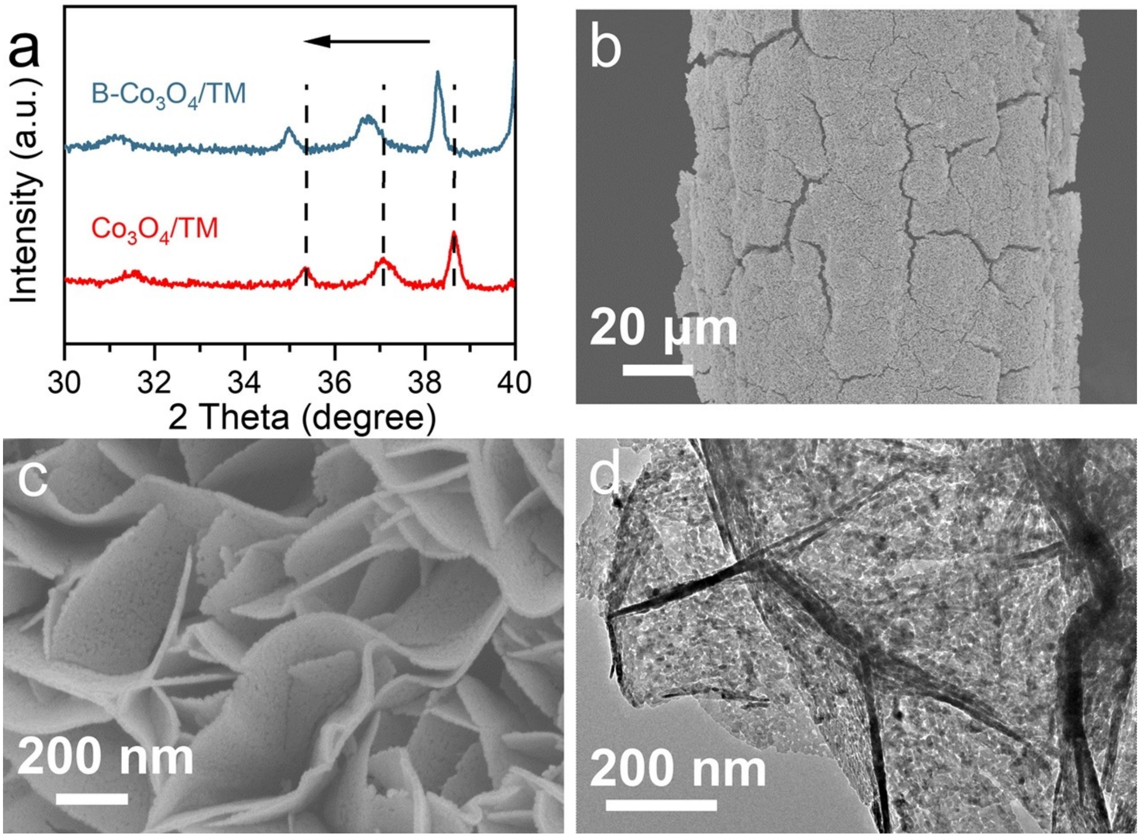

Fig. S1. (a) Partially enlarged XRD patterns of B-Co_3O_4/TM and Co_3O_4/TM. (b, c) SEM images of Co_3O_4/TM. (d) TEM image of Co_3O_4.

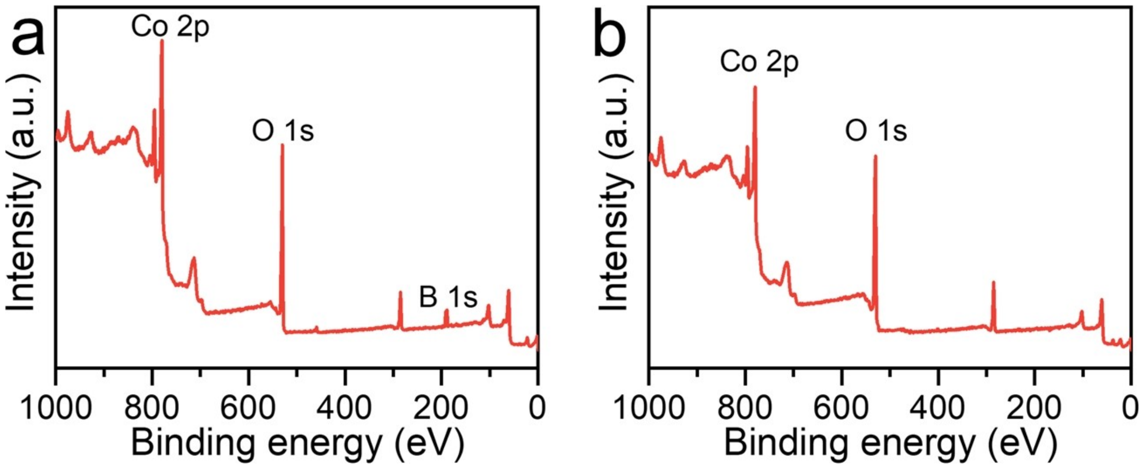

Fig. S2. The full spectra of XPS for (a) B-Co_3O_4/TM and (b) Co_3O_4/TM.

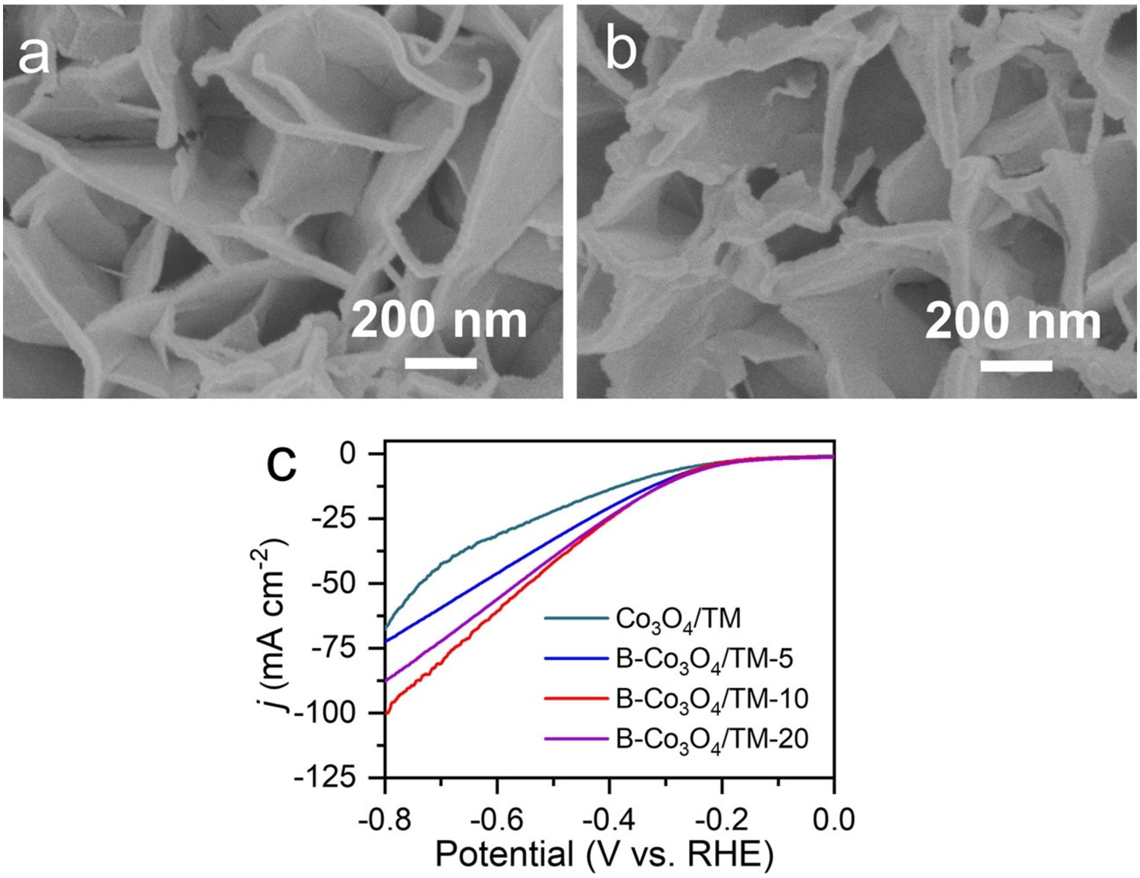

Fig. S3. SEM images of (a) B-Co_3O_4/TM-5 and (b) B-Co_3O_4/TM-20. (c) LSV curves in 0.1 M NaOH with 0.1 M NO_3^- for Co_3O_4/TM with different B doping amounts.

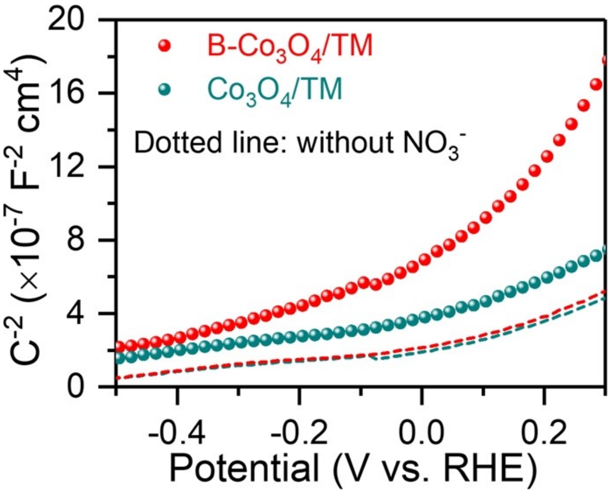

Fig. S4. M−S plots of the B-Co_3O_4/TM and Co_3O_4/TM with and without NO_3^-.

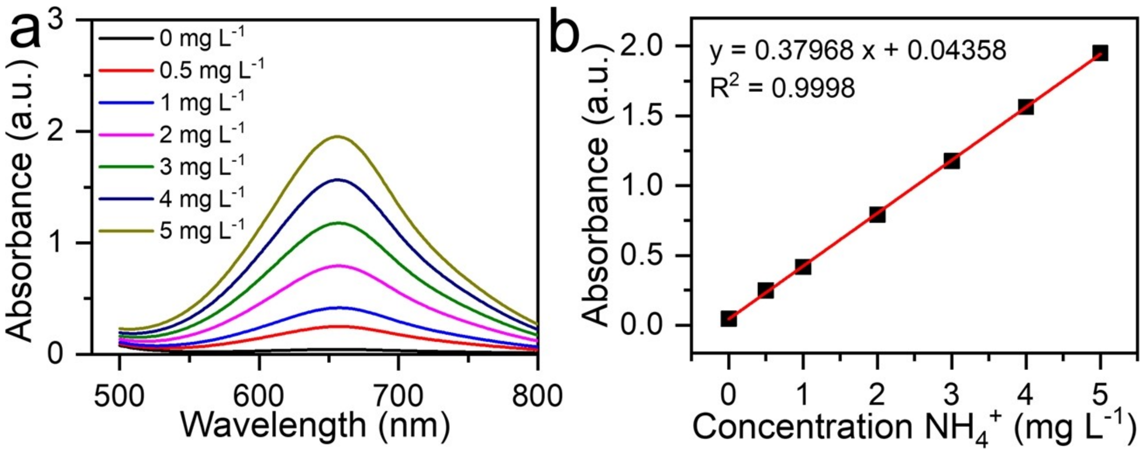

Fig. S5. (a) UV spectra and (b) calibration curve for determining NH_3.

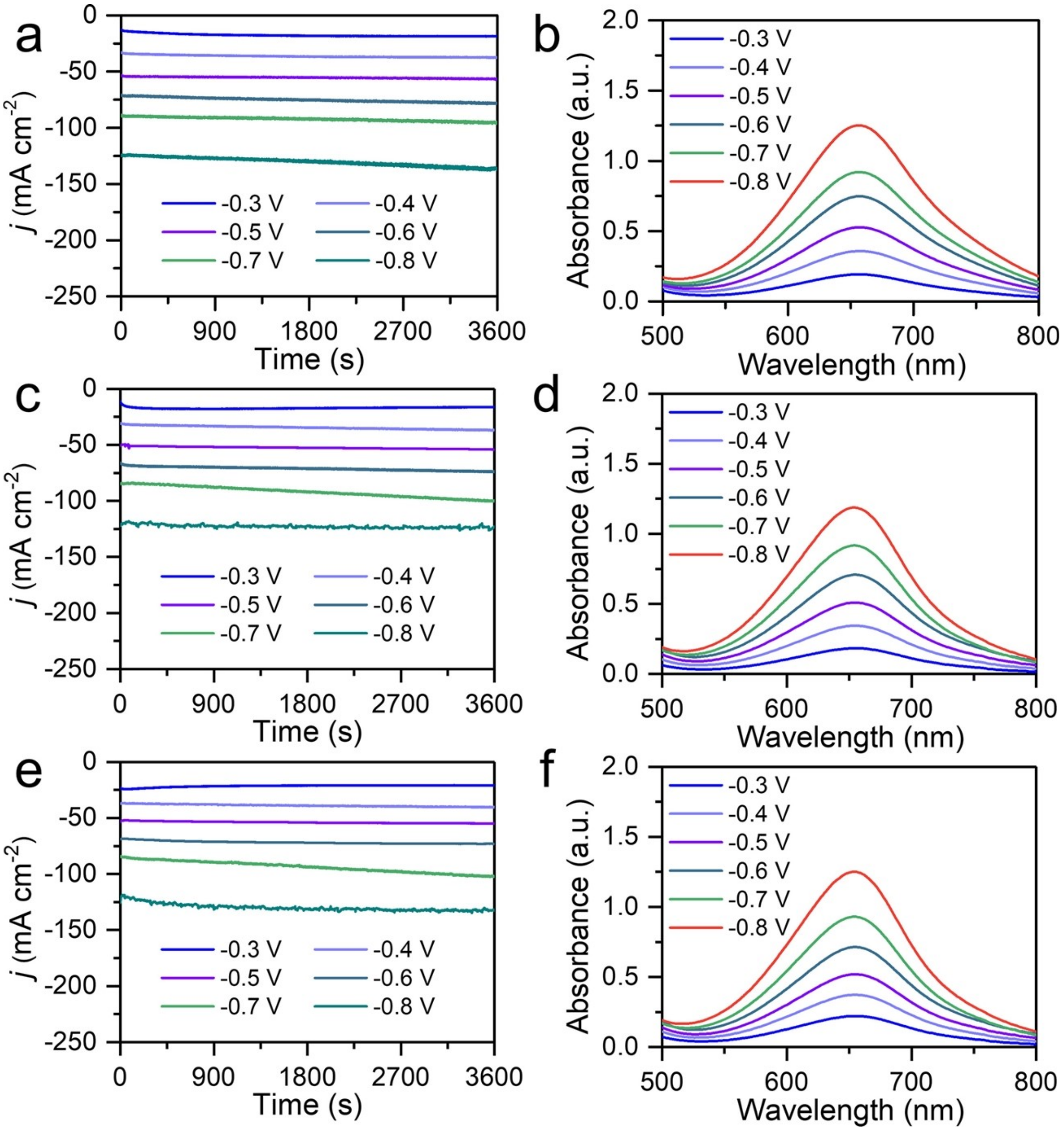

Fig. S6. (a, c, and e) Time-dependent current density curves and (b, d, and f) corresponding UV spectra of B-Co_3O_4/TM for the NO_3^-RR at different potentials.

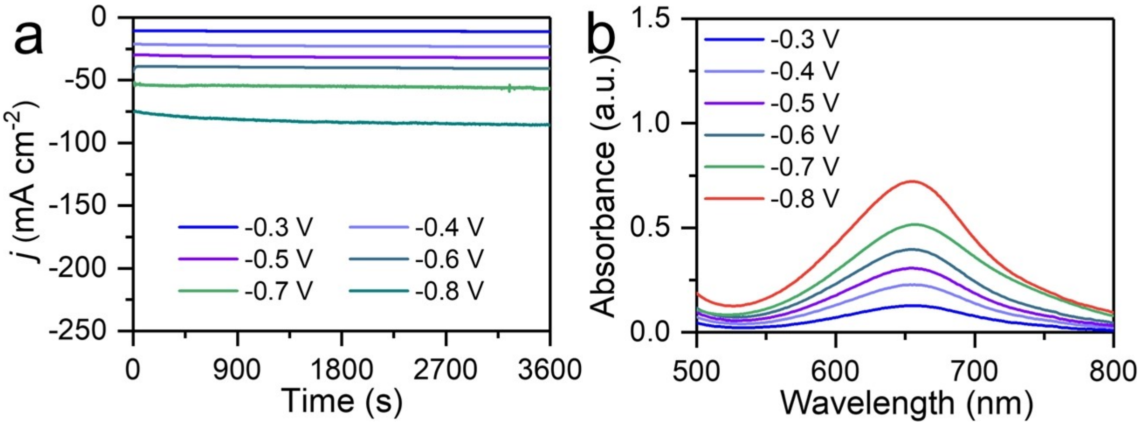

Fig. S7. (a) Time-dependent current density curves and (b) corresponding UV spectra of Co_3O_4/TM for the NO_3^-RR at different potentials.

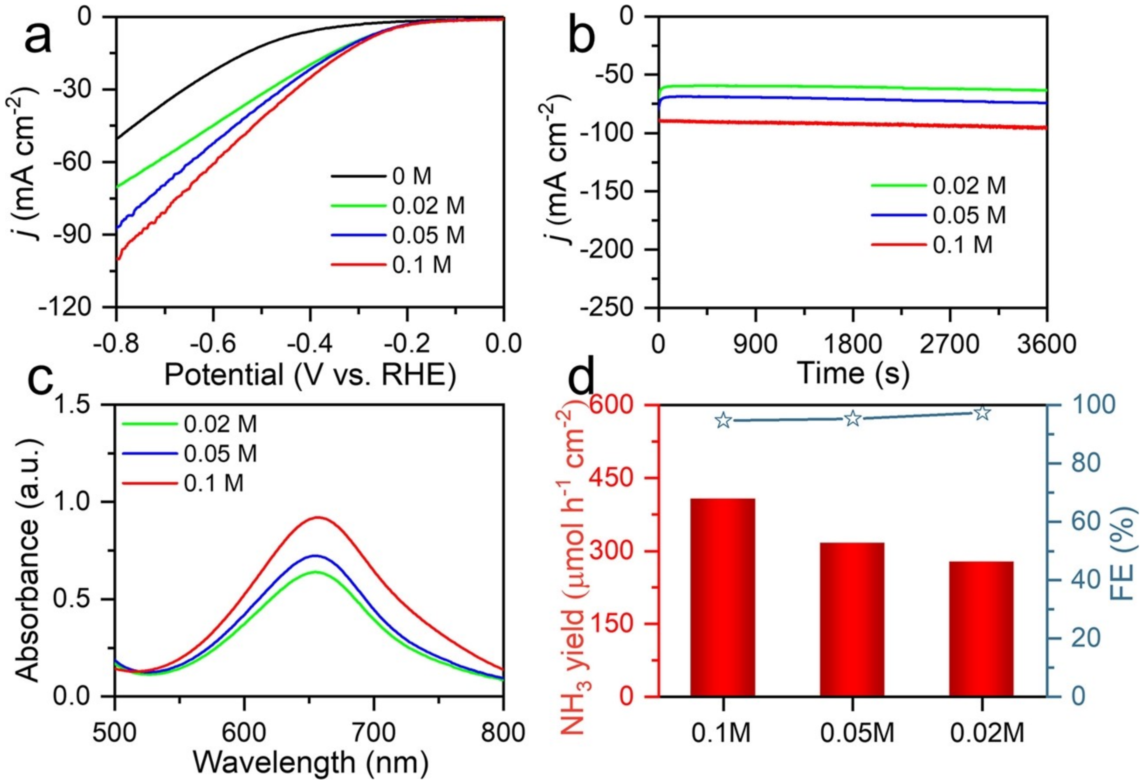

Fig. S8. (a) LSV curves, (b) time-dependent current density curves, (c) corresponding UV spectra, and (d) NH_3 yields and FEs of B-Co_3O_4/TM for the NO_3^-RR in 0.1 M NaOH with different NO_3^- concentrations at –0.7 V.

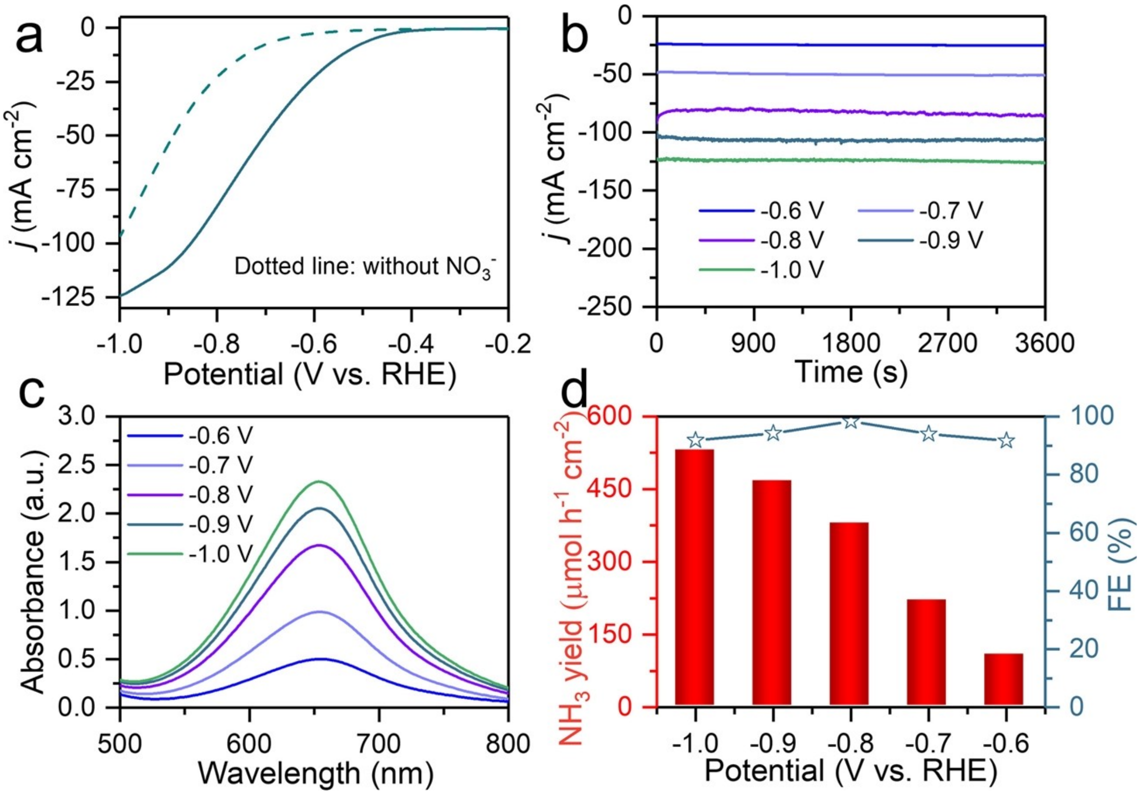

Fig. S9. (a) LSV curves, (b) time-dependent current density curves, (c) corresponding UV spectra, and (d) NH_3 yields and FEs of B-Co_3O_4/TM for the NO_3^-RR in 0.1 M PBS with 0.1 M NO_3^- at different potentials.

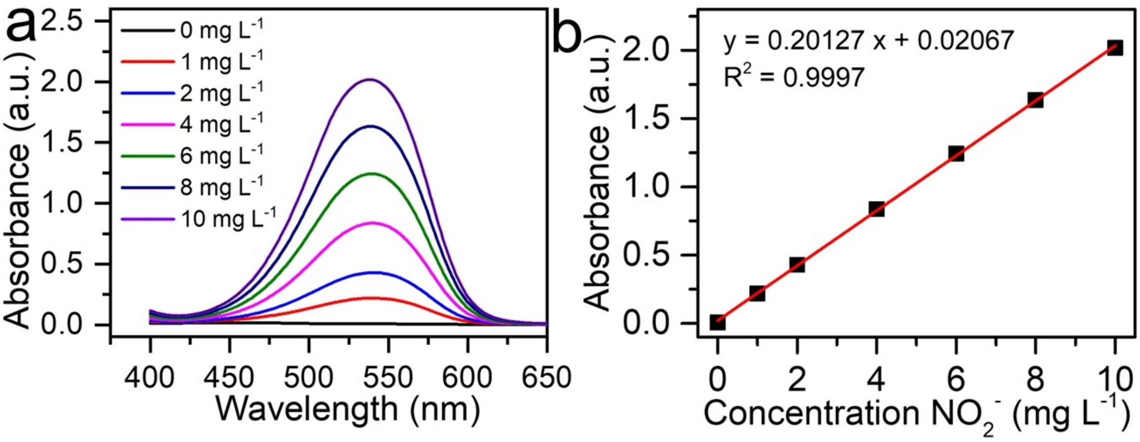

Fig. S10. (a) UV spectra and (b) calibration curve for determining NO_2^-.

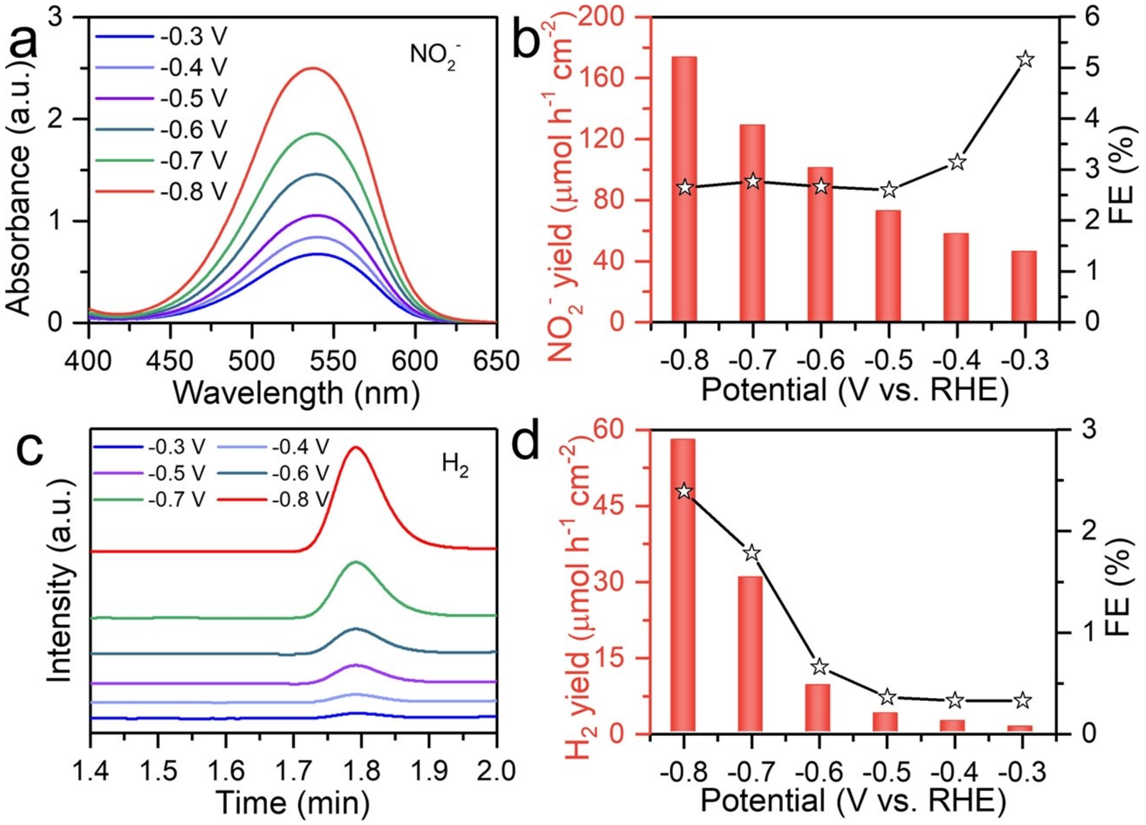

Fig. S11. (a) UV spectra and (b) yields and FEs of electrogenerated NO_2^-. (c) The H_2 spectra measured by GC and (d) yields and FEs of electrogenerated H_2 for B-Co_3O_4/TM at different potentials.

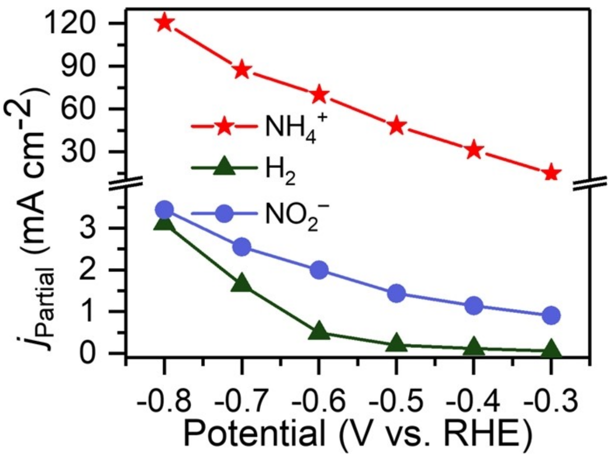

Fig. S12. Partial current densities of NH_4^+, NO_2^-, and H_2 for B-Co_3O_4/TM at different potentials.

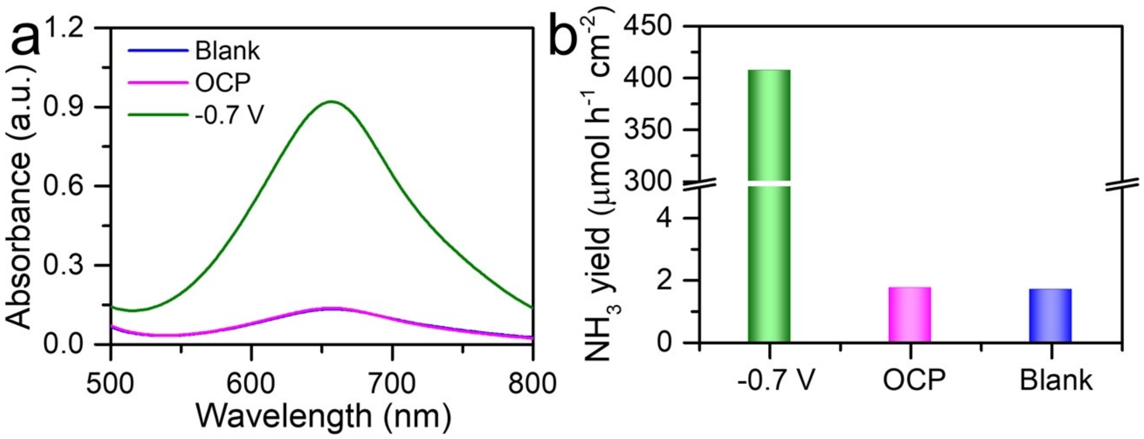

Fig. S13. (a) UV spectra and (b) yields of B-Co$_3$O$_4$/TM for the NO$_3^-$RR at different conditions.

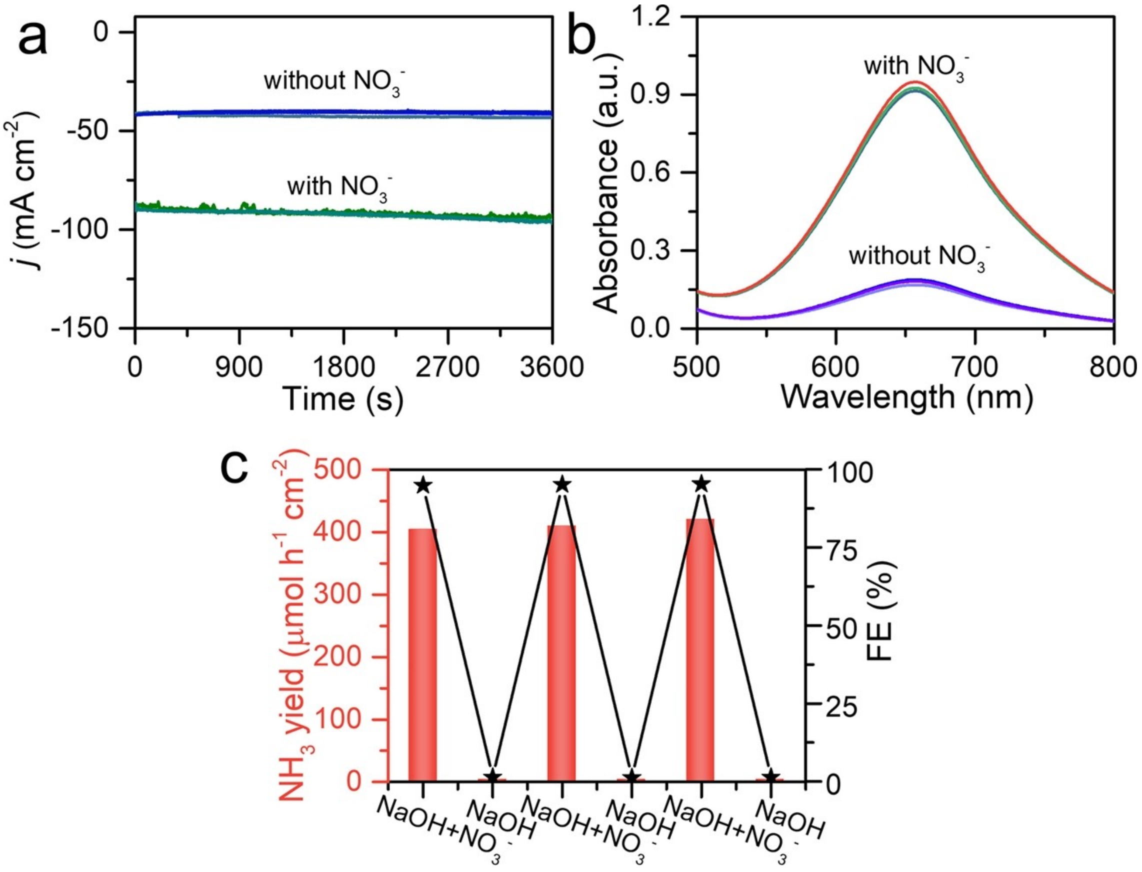

Fig. S14. (a) Time-dependent current density curves, (b) corresponding UV spectra, and (c) NH_3 yields and FEs of B-Co_3O_4/TM for during the alternating cycles tests between 0.1 M NaOH with and without 0.1 M NO_3^-.

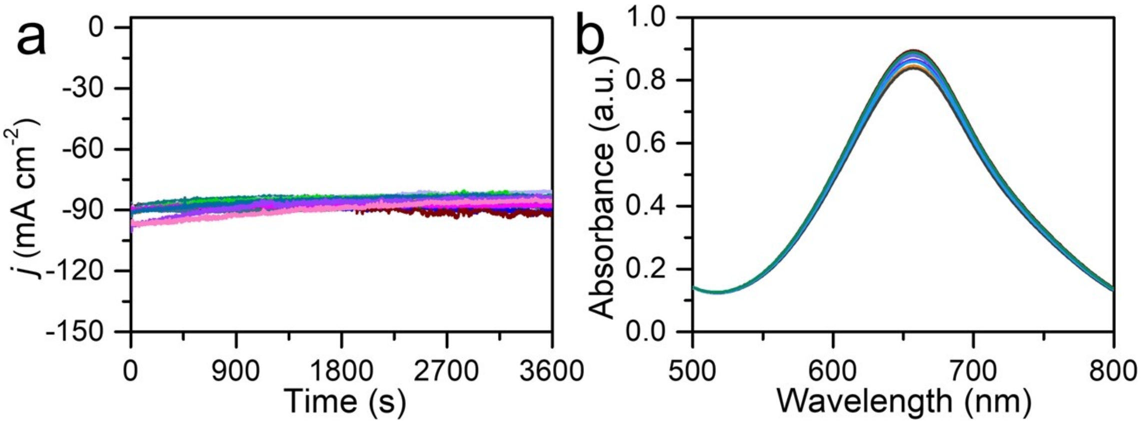

Fig. S15. (a) Time-dependent current density curves and (b) corresponding UV spectra of B-Co_3O_4/TM during recycling tests at −0.7 V.

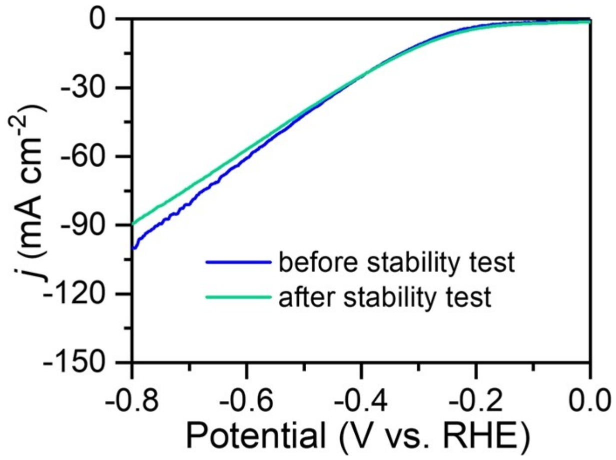

Fig. S16. LSV curves before and after long-time test for B-Co_3O_4/TM.

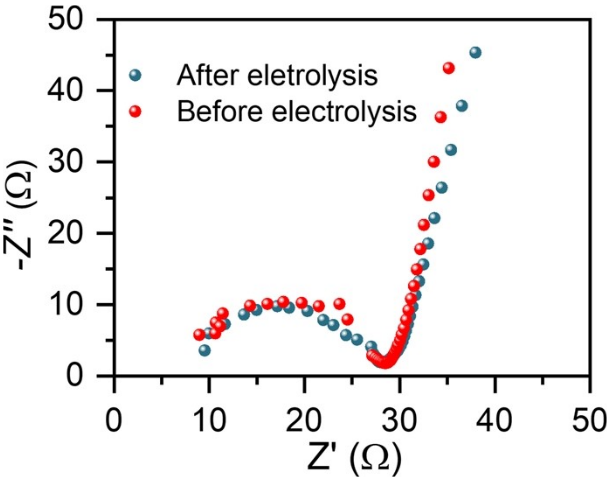

Fig. S17. EIS spectra for B-Co_3O_4/TM before and after the electrolysis.

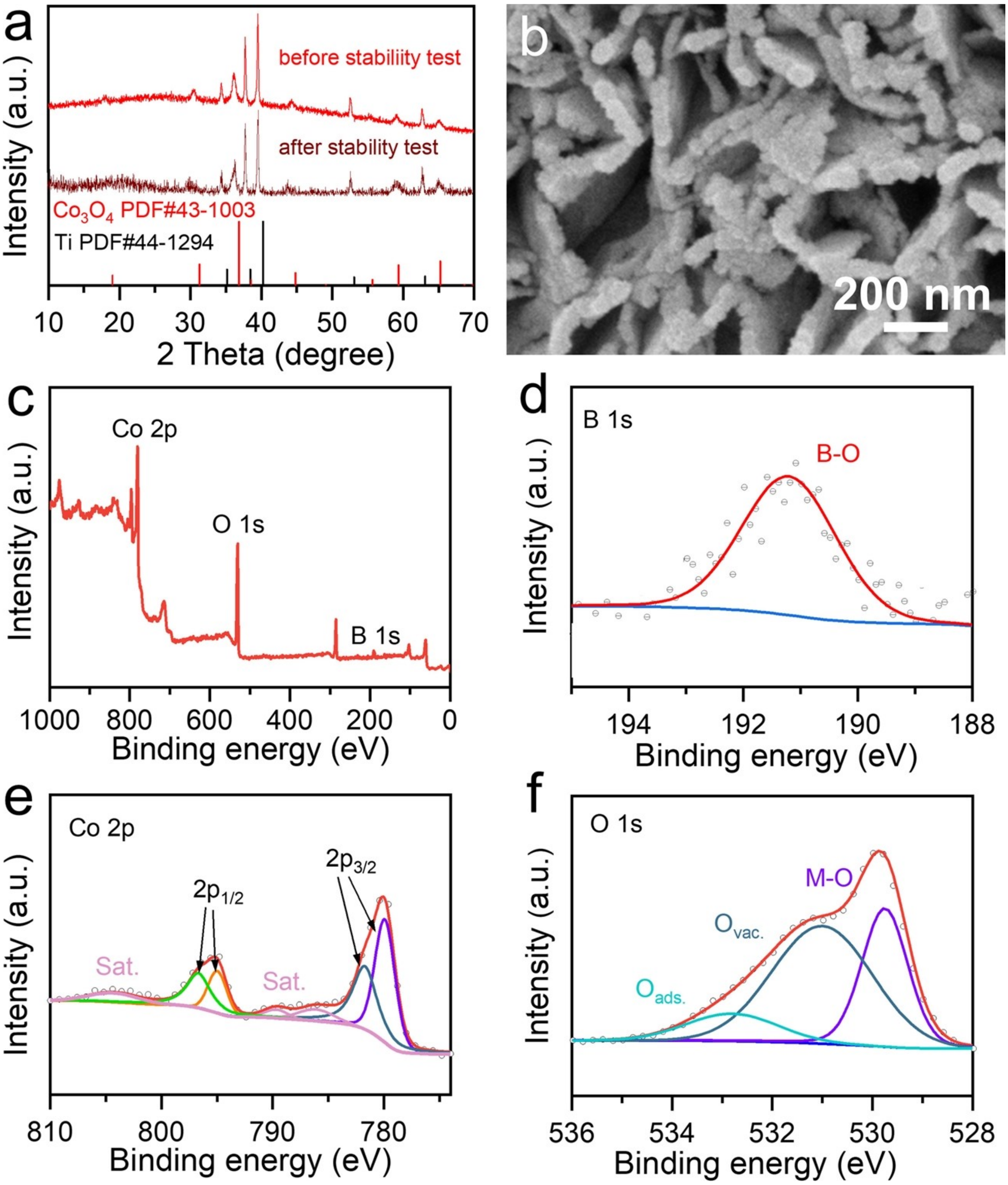

Fig. S18. (a) XRD pattern, (b) SEM image, high-resolution XPS spectra in (c) full spectrum, (d) B 1s region, (e) Co 2p region, and (f) O 1s region of B-Co_3O_4/TM after long-time test.

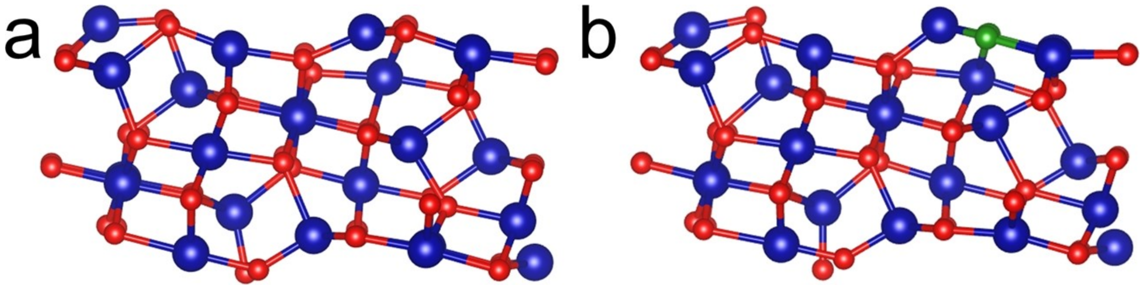

Fig. S19. Crystal structures of (a) Co_3O_4 and (b) B-Co_3O_4. Blue, red, and green spheres denote the Co, O, and B atoms, respectively.

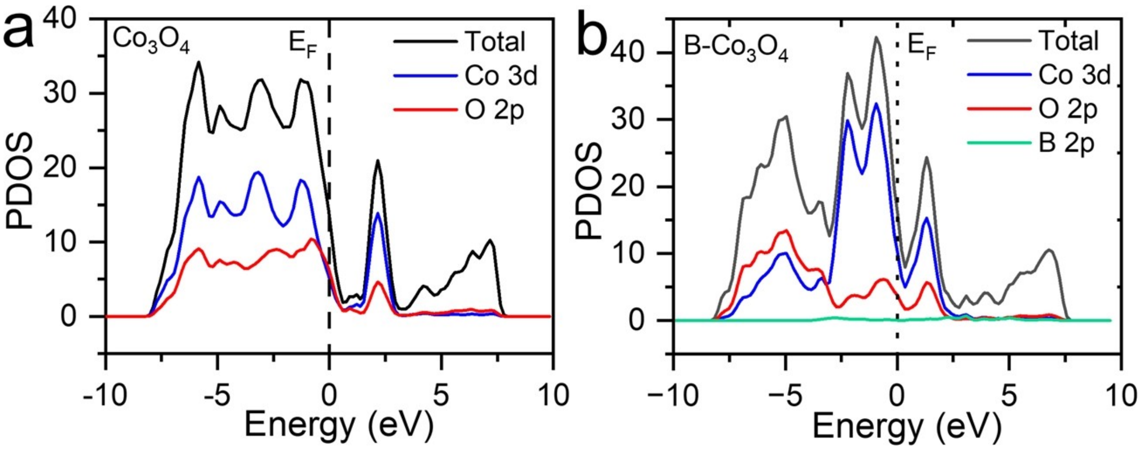

Fig. S20. Calculated PDOS of (a) Co_3O_4 and (b) B-Co_3O_4 configuration.

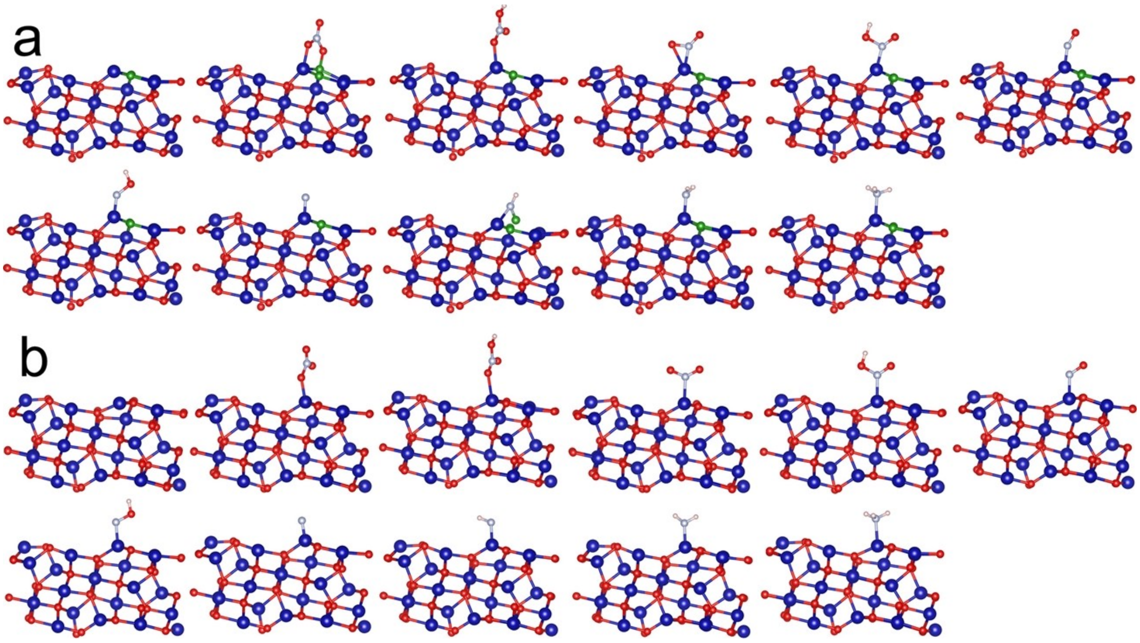

Fig. S21. Atomic structures of the reaction intermediates during the NO_3^-RR on the (a) B-Co_3O_4 and (b) Co_3O_4 surface. Blue, red, green, and silver spheres denote the Co, O, B, and N atoms, respectively.

Table S1. Comparison of catalytic performances for B-Co_3O_4/TM with other reported NO_3^-RR electrocatalysts.

Catalyst	Electrolyte	NH_3 yield @ Potential (μmol h^{-1} cm^{-2} @ V vs. RHE)	FE @ Potential (% @ V vs. RHE)	Ref.
B-Co_3O_4/TM	0.1 M NaOH (0.1 M NO_3^-)	407.3 @ −0.7	94.7 @ −0.7	This Work
O-Cu-PTCDA	0.1 M PBS (500 ppm NO_3^-)	25.65 @ −0.4	85.9 @ −0.4	[6]
Co-P/TP	0.2 M PBS (200 ppm NO_3^-)	24.47 @ −0.6	93.6 @ −0.3	[7]
NiFe hydroxide	0.1 M K_2SO_4 (200 ppm NO_3^-)	216 @ −0.75	74.8 @ −0.75	[8]
Mn_3O_4/CuO_x/CF	0.5 M Na_2SO_4 (200 ppm NO_3^-)	178.0 @ −0.85	86.55 @ −0.85	[9]
Cu_{SA}NPC	0.01 M PBS (500 ppm NO_3^-)	153 @ −1.1	87.2 @ −1.1	[10]
BC2N/Pd	0.1 M KOH (250 mM NO_3^-)	101.8 @ −0.7	97.42 @ −0.3	[11]
Co/CoO NSA	0.1 M Na_2SO_4 (200 ppm NO_3^-)	194.46 @ −0.65	93.8 @ −0.65	[12]
PdCoO/NF	0.5 M K_2SO_4 (200 ppm NO_3^-)	221.8 @ −1.5	88.6 @ −1.3	[13]
Fe SAC	0.10 M K_2SO_4 (0.50 M NO_3^-)	460 @ −0.85	75 @ −0.66	[14]
Rh NFs	0.1 M Na_2SO_4 (0.1 M NO_3^-)	13.5 @ 0.2	95 @ 0.2	[15]
Cu/Cu_2O NWAs	0.5 M Na_2SO_4 (200 ppm NO_3^-)	244.9 @ −0.85	95.8 @ −0.85	[16]
Ni_3N/N-C-800	0.5 M Na_2SO_4 (0.05 M NO_3^-)	277.5 @ −0.795	85 @ −0.795	[17]
PdMoCu	1 M KOH (0.1 M NO_3^-)	250.4 @ −0.6	56.95 @ −0.6	[18]
pCuO-5	0.05 M H_2SO_4 (0.05 M NO_3^-)	292 @ −0.6	89 @ −0.5	[19]
Fe-PPy SACs	0.1 M KOH (0.1 M NO_3^-)	161.76 @ −0.7	100 @ −0.5, −0.6	[20]
Ni_3B@$NiB_{2.74}$	0.1 M KOH (0.1 M NO_3^-)	198.3 @ −0.2	100 @ −0.2	[21]
$Cu_{50}Ni_{50}$/PTFE	1 M KOH (0.1 M NO_3^-)	/	99±1 @ −0.15	[22]
In-S-G	1 M KOH (0.1 M NO_3^-)	74.82 @ −0.5	75 @ −0.5	[23]
CoP NWAs/NF	0.2 M Na_2SO_4 (100 ppm NO_3^-)	/	99.4 @ −0.7	[24]
Cu@NF	1 M KOH (200 ppm NO_3^-)	252 @ −0.23	96.6 @ −0.23	[25]
Fe_2O_3 NRs/CC	0.5 M K_2SO_4 (0.1 M NO_3^-)	328.17 @ −0.9	69.76 @ −0.9	[26]
Pd-Co_3O_4/TM	0.1 M NaOH (0.1 M NO_3^-)	745.6 @ −0.6	98.7 @ −0.3	[27]
Co_3O_4-Mn_2	0.5 M K_2SO_4 (0.1 M NO_3^-)	2058.8 @ −1.2	99.5 @ −1.2	[28]
Pd/NF	0.5 M K_2SO_4 (0.1 M NO_3^-)	1520 @ −1.4	78 @ −1.4	[29]

Table S2. The relative contents of B-Co_3O_4/TM before and after electrolysis by XPS analysis.

Elements	Before electrolysis (at%)	After electrolysis (at%)
B	12.8	12.4
Co	16.2	15.1
O	42.4	44.0

References

1 G. Kresse and J. Hafner, Ab initio molecular-dynamics simulation of the liquid-metal-amorphous-semiconductor transition in germanium, *Phys. Rev. B*, 1994, **49**, 14251−14269.

2 J. P. Perdew, K. Burke and M. Ernzerhof, Generalized gradient approximation made simple, *Phys. Rev. Lett.*, 1996, **77**, 3865–3868.

3 M. Cococcioni and S. de Gironcoli, Linear response approach to the calculation of the effective interaction parameters in the LDA+U method, *Phys. Rev. B*, 2005, **71**, 035105.

4 H. J. Monkhorst and J. D. Pack, Special points for Brillonin-zone integrations. *Phys. Rev. B*, 1976, **13**, 5188−5192.

5 V. Wang, N. Xu, J. C. Liu, G. Tang and W. T. Geng, VASPKIT: a user-friendly interface facilitating high-throughput computing and analysis using VASP code. *Comput. Phys. Commun.*, 2021, **267**, 108033.

6 G. F. Chen, Y. Yuan, H. Jiang, S. Y. Ren, L. X. Ding, L. Ma, T. Wu, J. Lu and H. Wang, Electrochemical reduction of nitrate to ammonia via direct eight-electron transfer using a copper-molecular solid catalyst, *Nat. Energy*, 2020, **5**, 605−613.

7 Z. Li, G. Wen, J. Liang, T. Li, Y. Luo, Q. Kong, X. Shi, A. M. Asiri, Q. Liu and X. Sun, High-efficiency nitrate electroreduction to ammonia on electrodeposited cobalt-phosphorus alloy film. *Chem. Commun.*, 2021, **57**, 9720−9723.

8 X. Wu, A. Ma, J. Hu, D. Liu, A. T. Kuvarega, B. B. Mamba and J. Gui, Amorphous nickel–iron hydroxide nanosheets for effective electroreduction of nitrate to ammonia. *Inorg. Chem. Front.*, 2023, **10**, 666−674.

9 J. Hu, A. Ma, X. Wu, Y. Yin, D. Liu, A. T. Kuvarega, B. B. Mamba and J. Gui, Mn_3O_4/CuO_x heterostructure for nitrate electroreduction to ammonia. *Chem. Commun.*, 2023, **59**, 7232−7235.

10 X. Zhao, Q. Geng, F. Dong, K. Zhao, S. Chen, H. Yu and X. Quan, Boosting the selectivity and efficiency of nitrate reduction to ammonia with a single-atom Cu electrocatalyst, *Chem. Eng. J.*, 2023, **466**, 143314.

11 X. Li, X. Zhao, Y. Zhou, J. Hu, H. Zhang, X. Hu and G. Hu, Pd nanocrystals embedded in BC2N for efficient electrochemical conversion of nitrate to ammonia. *Appl. Surf. Sci.*, 2023, **584**, 152556.

12 Y. Yu, C. Wang, Y. Yu, Y. Wang and B. Zhang, Promoting selective electroreduction of nitrates to ammonia over electron-deficient Co modulated by rectifying Schottky contacts. *Sci. China Chem.*, 2020, **63**, 1469−1476.

13 M. Liu, Q. Mao, K. Shi, Z. Wang, Y. Xu, X. Li, L. Wang and H. Wang, Electroreduction of nitrate to ammonia on palladium−cobalt−oxygen nanowire arrays. *ACS Appl. Mater. Interfaces*, 2022, **14**, 13169−13176.

14 Z. Y. Wu, M. Karamad, X. Yong, Q. Huang, D. A. Cullen, P. Zhu, C. Xia, Q. Xiao, M. Shakouri, F. Y. Chen, J. Y. T. Kim, Y. Xia, K. Heck, Y. Hu, M. S. Wong, Q. Li, I. Gates, S. Siahrostami and H. Wang, Electrochemical ammonia synthesis via nitrate reduction on Fe single atom catalyst. *Nat. Commun.* 2021, **12**, 2870.

15 H. Liu, J. Timoshenko, L. Bai, Q. Li, M. Rüscher, C. Sun, B. R. Cuenya and J. Luo, Low-coordination rhodium catalysts for an efficient electrochemical nitrate reduction to ammonia. *ACS Catal.*, 2023, **13**, 1513−1521.

16 Y. Wang, W. Zhou, R. Jia, Y. Yu and B. Zhang, Unveiling the activity origin of a copper-based electrocatalyst for selective nitrate reduction to ammonia. *Angew. Chem. Int. Ed.*, 2020, **59**, 5350−5354.

17 X. Zhang, G. Ma, L. Shui, G. Zhou and X. Wang, Ni_3N nanoparticles on porous nitrogen-doped carbon nanorods for nitrate electroreduction. *Chem. Eng. J.*, 2022, **430**, 132666.

18 X. Tong, Z. Zhang, Z. Fang, J. Guo, Y. Zheng, X. Liang, R. Liu, L. Zhang and W. Chen, PdMoCu trimetallenes for nitrate electroreduction to ammonia. *J. Phys. Chem. C*, 2023, **127**, 5262−5270.

19 R. Daiyan, T. Tran-Phu, P. Kumar, K. Iputera, Z. Tong, J. Leverett, M. H. A. Khan, A. A. Esmailpour, A. Jalili, M. Lim, A. Tricoli, R. S. Liu, X. Lu, E. Lovell and R. Amal, Nitrate reduction to ammonium: from CuO defect engineering to waste NO_x-to-NH_3 economic feasibility. *Energy Environ. Sci.*, 2021, **14**, 3588−3598.

20 P. Li, Z. Jin, Z. Fang and G. Yu, A single-site iron catalyst with preoccupied active centers that achieves selective ammonia electrosynthesis from nitrate. *Energy Environ. Sci.*, 2021, **14**, 3522−3531.

21 L. Li, C. Tang, X. Cui, Y. Zheng, X. Wang, H. Xu, S. Zhang, T. Shao, K. Davey and S. Z. Qiao, Efficient nitrogen fixation to ammonia through integration of

plasma oxidation with electrocatalytic reduction. *Angew. Chem. Int. Ed.*, 2021, **60**, 14131−14137.

22 Y. Wang, A. Xu, Z. Wang, L. Huang, J. Li, F. Li, J. Wicks, M. Luo, D. H. Nam, C. S. Tan, Y. Ding, J. Wu, Y. Lum, C. T. Dinh, D. Sinton, G. Zheng and E. H. Sargent, Enhanced nitrate-to-ammonia activity on copper-nickel alloys via tuning of intermediate adsorption. *J. Am. Chem. Soc.*, 2020, **142**, 5702−5708.

23 F. Lei, W. Xu, J. Yu, K. Li, J. Xie, P. Hao, G. Cui and B. Tang, Electrochemical synthesis of ammonia by nitrate reduction on indium incorporated in sulfur doped graphene, *Chem. Eng. J.*, 2021, **426**, 131317.

24 Y. Gao, R. Wang, Y. Li, E. Han, M. Song, Z. Yang, F. Guo, Y. He and X. Yang, Regulating dynamic equilibrium of active hydrogen for super-efficient nitrate electroreduction to ammonia. *Chem. Eng. J.*, 2023, **474**, 145546.

25 J. Li, J. Gao, T. Feng, H. Zhang, D. Liu, C. Zhang, S. Huang, C. Wang, F. Du, C. Li and C. Guo, Effect of supporting matrixes on performance of copper catalysts in electrochemical nitrate reduction to ammonia. *J. Power Sources*, 2021, **511**, 230463.

26 T. Li, C. Tang, H. Guo, H. Wu, C. Duan, H. Wang, F. Zhang, Y. Cao, G. Yang and Y. Zhou, In situ growth of Fe_2O_3 nanorod arrays on carbon cloth with rapid charge transfer for efficient nitrate electroreduction to ammonia. *ACS Appl. Mater. Interfaces,* 2022, **14**, 49765−49773.

27 X. Fan, C. Liu, Z. Li, Z. Cai, L. Ouyang, Z. Li, X. He, Y. Luo, D. Zheng, S. Sun, Yan Wang, B. Ying, Q. Liu, A. Farouk, M. S. Hamdy, F. Gong, X. Sun and Y.

Zheng, Pd-doped Co_3O_4 nanoarray for efficient eight-electron nitrate electrocatalytic reduction to ammonia synthesis. *Small*, 2023, **19**, 2303424.

28 D. Liu, L. Qiao, Y. Chen, P. Zhou, J. Feng, C. C. Leong, K. W. Ng, S. Peng, S. Wang, W. F. Ip and H. Pan, Electrocatalytic reduction of nitrate to ammonia on low-cost manganese-incorporated Co_3O_4 nanotubes. *Appl. Catal. B*, 2023, **324**, 122293.

29 H. Guo, M. Li, Y. Yang, R. Luo, W. Liu, F. Zhang, C. Tang, G. Yang and Y. Zhou, Self-supported Pd nanorod arrays for high-efficient nitrate electroreduction to ammonia. *Small*, 2023, **19**, 2207743.